Research article

Corrosion behavior of Ti–Pt-coated stainless steel for bipolar plates in polymer electrolyte membranes under water electrolysis conditions

Sin-Jae Kang [a], Geon-Il Kim [a], Seung-Hyun Kim [a], Ji-Han Lee [b], Jeong-Soo Kim [b], Seong-Un Im [b], Yeon-Soo Kim [b], Jung-Gu Kim [a,*]

[a] School of Advanced Materials Science and Engineering, Sungkyunkwan University, 300 Chunchun-Dong, Jangan-Gu, Suwon-si, Gyeonggi-do, 16419, South Korea
[b] Water Electrolyzer Engineering Design Team, R&D Division, Hyundai Motor Company, 17-5, Mabuk-ro 240 beongil, Giheung-gu, Yongin-si, Gyeonggi-do, 16891, South Korea

ARTICLE INFO

ABSTRACT

In this study, the corrosion behavior and degradation mechanism of Ti–Pt-coated stainless steel bipolar plates were investigated through electrochemical tests and surface analysis in a polymer electrolyte membrane water electrolysis (PEMWE) operating environment. The coated bipolar plate has a corrosion current density of only 1.68×10^{-8} A/cm^2, which is an order of magnitude lower than that of the bare SS316L substrate (1.94×10^{-7} A/cm^2), indicating that its corrosion resistance is superior to that of bare SS316L substrate. However, in the PEMWE operating environment, the protection efficiency of the coating and the corrosion resistance of the coated bipolar plate decreased. The degradation of the coated bipolar plate can be attributed to electrolyte penetration into the blistering areas of the coating layer with micro voids. Defects in the coating layer occur because of the pressure of oxygen gas generated within the coating layer under high-potential conditions, thereby exposing the substrate to the electrolyte and corrosion.

1. Introduction

With growing concerns regarding climate change caused by the excessive use of fossil fuels, interest in the development of alternative energy sources, such as solar and wind energies, is increasing [1–4]. Unlike other renewable energies, hydrogen energy can stably generate electricity regardless of weather or climate conditions, and it can be produced in an ecofriendly manner without concerns of depletion or regional imbalance. Furthermore, hydrogen can be stored in the form of a liquid or a high-pressure gas, making it easy to transport. Because of these advantages, hydrogen has attracted attention as a feasible alternative energy source [5–10]. Among various hydrogen production technologies, water electrolysis is the most environmentally friendly method because it produces hydrogen without emitting pollutants, such as greenhouse gases, because of the use of renewable energy sources such as solar and wind power [11,12].

Polymer electrolyte membrane water electrolysis (PEMWE) is a promising hydrogen production technology among various water electrolysis methods. Furthermore, it is being actively researched and developed because of its various advantages, such as high

---

* Corresponding author.
  E-mail address: kimjg@skku.edu (J.-G. Kim).

current density operations (1.0–2.0 A/cm^2), high-purity hydrogen production in high-pressure and differential pressure environments, low gas permeability, excellent fast start-up/shutdown responsiveness, and component miniaturization applications [13–19]. Bipolar plates are a crucial component of the PEMWE stack and have various functions, including cell separation, current and heat transfer between cells, separation of hydrogen, oxygen, and cooling water, and supporting cells [20,21]. A bipolar plate should have high mechanical strength, electrical conductivity, thermal conductivity, and corrosion resistance [22,23]. In particular, the high corrosion resistance of bipolar plates helps them withstand the harsh operating environment of PEMWE, which involves high overpotential (1.6–2.0 V), hot environments (T = 60°C-80 °C), and acidic environments (pH = 1–4) [24,25]. Therefore, to withstand such harsh environments, high corrosion-resistant metals, such as high-purity titanium, are used as bipolar plate materials [16,26,27]. The use of expensive materials in bipolar plates, accounting for 51 % of the cost of the PEMWE stack, contributes to its high manufacturing cost [28]. As an alternative, stainless steel has been suggested as a potential candidate to replace expensive metals used in bipolar plates for PEMWE to reduce the high manufacturing cost of PEMWE. Stainless steel has better machinability than titanium, making it more useful for designing complicated flow fields in bipolar plates. It also has a lower manufacturing cost than more difficult-to-machine titanium. Furthermore, stainless steel has superior formability compared with magnesium alloys and has greater corrosion resistance than copper and aluminum alloys [26,29–33]. However, despite these advantages of stainless steel, it is susceptible to corrosion in high-overpotential environments [34]. Moreover, iron ions released during the corrosion process can poison the membrane electrode assembly of PEMWE [35,36].

To overcome this drawback, many researchers have proposed the use of coated bipolar plates, where highly corrosion-resistant materials, such as gold, niobium, TiN, CrN, and platinum, are used to coat stainless steel [37–41]. Although many studies have been conducted on the coating of stainless steel bipolar plates with various corrosion-resistant metals for PEMWE, research on the degradation mechanism and corrosion characteristics of the coated bipolar plates under PEMWE operation conditions is insufficient. Therefore, it is essential to accurately understand the corrosion characteristics of coated bipolar plates and investigate their degradation mechanisms in PEMWE operating environments.

In this study, potentiodynamic polarization tests and electrochemical impedance spectroscopy (EIS) were performed before and after potentiostatic polarization tests to evaluate the corrosion characteristics of a coated bipolar plate. Potentiostatic polarization tests were conducted to analyze the corrosion behavior of the coated bipolar plate at the operating potential of a PEMWE cell. We analyzed the surface condition of the coated bipolar plate before and after the potentiostatic polarization tests using optical microscopy (OM), scanning electron microscopy (SEM), energy-dispersive X-ray spectroscopy (EDS), and auger electron spectroscopy (AES). Furthermore, *in situ* OM monitoring was performed during the potentiostatic polarization tests to verify real-time changes in the plate surface and thus derive the corrosion mechanism. Finally, we verified the degradation mechanism of the coated bipolar plate through oxygen generation experiments.

2. Materials and methods

2.1. Specimen

In this study, 316L stainless steel was used as the substrate material with a thickness of ~80 μm. Before magnetron sputtering, all substrate materials were polished using up to 1200-grit sandpapers. Subsequently, all 316L stainless steel materials were washed with ethanol and distilled water. Pure metal titanium and platinum were used as target materials to form a coating layer on the 316L stainless steel substrate under Ar (99.999 %) atmosphere. Before deposition, the chamber pressure was pumped below ~7.5 × 10^{-4} torr and the substrate temperature was maintained at 25 °C. Furthermore, the substrate was cleaned using Ar ions with a negative bias voltage of −700 V to remove the oxide film and impurities on the surface. The power used for the target materials was 360 W, and the coating process yielded approximately a 350-nm titanium layer and a 50-nm platinum layer (Fig. S1).

2.2. Electrochemical tests

The corrosion properties of the specimens were evaluated using potentiodynamic polarization, potentiostatic polarization, and EIS tests. All electrochemical tests were conducted in a three-electrode system using a VSP-300 (Bio-Logic SAS, Seyssinet-Pariset, France). The specimens were connected to a working electrode; two pure graphite rods were used as the counter electrode, and a saturated calomel electrode with a Luggin capillary was used as the reference electrode. The area of the test specimen exposed to electrolytes was 1 cm^2. All experiments were conducted in an aerated 0.05-M H$_2$SO$_4$ solution containing 2 ppm of fluoride ions (pH = 1.25). The temperature was maintained at 65 °C to reflect the temperature of the PEMWE system. Before the potentiodynamic and potentiostatic polarization tests, the specimen was kept in the solution for 24 h to establish the open-circuit potential (OCP). Potentiodynamic polarization tests were conducted from −250 mV (vs. OCP) to 1800 mV$_{SCE}$ at a potential sweep rate of 0.166 mV/s. A potentiostatic polarization test was conducted to simulate the potential applied to the bipolar plates on the anode side of an operating PEMWE cell. The coated bipolar plate and bare SS316L were maintained at 1.76 V$_{SCE}$ (2 V$_{SHE}$) for 3 h to analyze their corrosion behavior under the PEMWE operation conditions. EIS measurements were performed in the frequency range of 100 kHz–10 mHz with an amplitude of 10 mV. Moreover, the impedance plots were interpreted with respect to an equivalent circuit using a fitting procedure performed using the ZSimpWin software (ZSimpWin 3.20, Echem Software, Warminster, PA, USA).
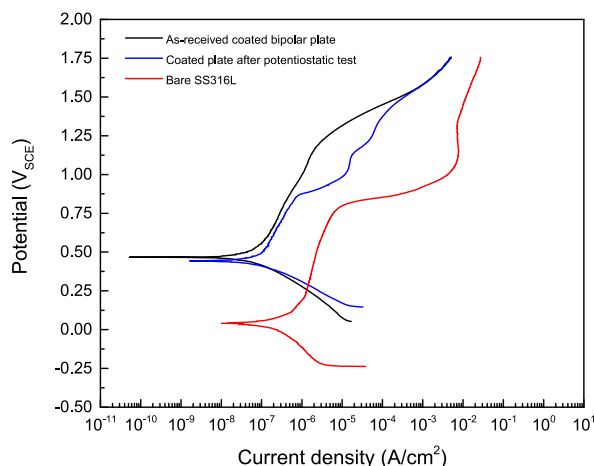
Fig. 1. Potentiodynamic polarization curves of coated bipolar plates and SS316L substrate.

Table 1
Potentiodynamic polarization parameters of the substrate and coated bipolar plates.

	E_{corr} (V_{SCE})	i_{corr} (A/cm^2)	β_a (V/decade)	β_c (V/decade)	R_p ($\Omega \cdot$cm^2)	Porosity (P)	P_i
SS316L	0.041	1.94×10^{-7}	0.336	0.231	3.06×10^5	–	–
As-received bipolar plate	0.468	1.68×10^{-8}	0.170	0.068	1.26×10^6	0.013	92 %
Bipolar plate after the potentiostatic test	0.443	5.4×10^{-8}	0.165	0.076	4.19×10^5	0.046	72 %

2.3. Surface analyses

Surface analysis of the experimental specimens was performed before and after the potentiostatic polarization tests. The morphologies and cross-sectional images of the specimens were observed using OM (DM 2700 M, Leica, Wetzlar, Germany), SEM, and EDS (JSM-7900F, JEOL Ltd., Tokyo, Japan) to verify the degradation mechanism of the coated bipolar plate during PEMWE cell operation. Furthermore, the composition of the interior of the coating defects was observed using AES depth profiling (JAMP-9500F, JEOL Ltd, Tokyo, Japan). Compositional sputter depth profiling was performed by etching with 3-keV argon ions while observing the elemental peaks for Ti, Fe, Cr, Ni, and Pt. The chamber vacuum was maintained below 6.7×10^{-8} Pa. In addition, during the potentiostatic polarization test, the bipolar plate surface was monitored *in situ* via OM.

2.4. Oxygen generation experiment

An oxygen generation experiment was conducted to verify the degradation mechanism of the coated bipolar plates by comparing the theoretical volume of generated oxygen with the experimentally obtained oxygen volume. Next, a potentiostatic polarization test was conducted using a three-electrode system by applying 1.76 V_{SCE} (2 V_{SHE}) for 3 h to generate oxygen gas. The generated gas was captured by displacement with water, and the amount of corrosion of the bipolar plate was measured by weighing it before and after the potentiostatic polarization test.

3. Results and discussion

3.1. Electrochemical tests

3.1.1. Potentiodynamic polarization
Fig. 1 shows the potentiodynamic polarization curves for the as-received coated bipolar plate, the coated bipolar plate after the potentiostatic polarization test, and the SS316L substrate. Table 1 lists the electrochemical parameters obtained from the potentiodynamic polarization curves for the SS316L substrate, the as-received coated bipolar plate, and the coated bipolar plate after the potentiostatic polarization test. The polarization resistance (R_p) was determined by the following Eq. (1) [42]:

$$R_p = \frac{\beta_a \beta_c}{2.3\, i_{corr}(\beta_a + \beta_c)}, \tag{1}$$

where β_a and β_c denote the anodic and cathodic Tafel slopes, respectively, and i_{corr} denotes the corrosion current density. In the case of
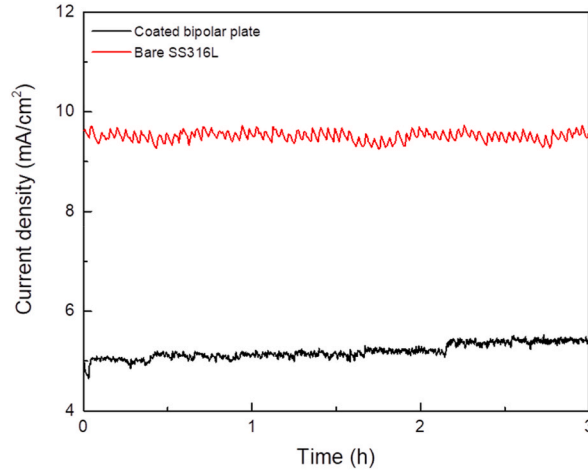
Fig. 2. Current density of coated bipolar plate and bare SS316L over time at E_{app} = 1.76 V_{SCE}.

the as-received coated bipolar plate, the current density increases at approximately 1.2 V_{SCE} without pitting potential. As the potential is sufficiently high to cause an oxygen evolution reaction (OER), the current density increases with an increase in this potential because of the occurrence of the OER instead of the corrosion reaction on the platinum surface, which is the top coating layer of the bipolar plate [43]. All coated bipolar plates (0.468 V_{SCE}, 0.443 V_{SCE}) exhibit more positive corrosion potentials (E_{corr}) than the SS316L substrate (0.041 V_{SCE}) because the top platinum coating layer exhibits a more noble corrosion potential than SS316L. Furthermore, all coated bipolar plates exhibit lower corrosion current density (i_{corr}) than the SS316L substrate. The as-received coated bipolar plate has a corrosion current density of only 1.68×10^{-8} A/cm^2, which is an order of magnitude lower than that of the bare SS316L substrate (1.94×10^{-7} A/cm^2). In addition, the polarization resistance of the as-received coated bipolar plate is four times higher than that of the bare SS316L substrate. These results confirm that the coating of the bipolar plates results in superior corrosion resistance compared with that of the SS316L substrate. Porosity of the coating can be derived from the measured polarization resistance. The porosity of the coating was determined using the following Eq. (2) [44,45]:

$$P = \frac{R_p^0}{R_p} \times 10^{-|\Delta E_{corr}|/\beta_a},$$ (2)

where P represents the total coating porosity; R_p^0 denotes the polarization resistance of the substrate; R_p denotes the measured polarization resistance of the coated bipolar plate; ΔE_{corr} denotes the difference in the corrosion potential between the coated bipolar plate and substrate; β_a denotes the anodic Tafel slope of the substrate. The porosity of the coated bipolar plate after the potentiostatic polarization test increased approximately four times compared with that of the as-received bipolar plate. These results demonstrate that defects occur on the coating layer of the coated bipolar plate after the potentiostatic polarization test, thereby reducing the corrosion resistance of the coated bipolar plate compared with that of the as-received bipolar plate. In addition, the protective efficiency (P_i) of the coating can be determined using the following Eq. (3) [46]:

$$P_i = 100 \times \left(1 - \frac{i_{corr}}{i_{corr}^0}\right),$$ (3)

where i_{corr} and i_{corr}^0 denote the corrosion current densities in the presence and absence of coating, respectively. The protective efficiency of the coating of the as-received bipolar plate was 92 %. However, after the potentiostatic polarization test, the protective efficiency of the coating decreased by 72 %, indicating reduced corrosion resistance of the bipolar plate because of defects in the coating layer.

3.1.2. Potentiostatic polarization test

The potentiostatic polarization test was conducted at 1.76 V_{SCE} (2 V_{SHE}) for 3 h to analyze the corrosion behavior of the coated bipolar plate and bare SS316L under PEMWE operation conditions. Fig. 2 shows the potentiostatic polarization test results for 3 h. When an overpotential of 1.76 V_{SCE} (2 V_{SHE}) was applied to the bipolar plate, a high current density of over 5 mA/cm^2 was observed. The high current density can be attributed to the reaction of oxygen generation on the platinum surface, which is the top coating of the bipolar plate under high-overpotential conditions [43]. Furthermore, the current density gradually increased from 5 to 5.52 mA/cm^2 over time. Conversely, when an overpotential of 1.76 V_{SCE} (2 V_{SHE}) was applied to bare SS316L, a stabilized current density was observed. This occurs because the high-overpotential (1.76 V_{SCE}) and low-pH conditions lead to the rapid dissolution of Cr and Fe in the passivation layer of stainless steel, causing the breakdown of passivation and resulting in uniform corrosion across the entire surface of the exposed bare SS316L substrate in the electrolyte [47]. Therefore, this result indicates that after the SS316L substrate was exposed to the electrolyte because of the increase in the number of defects in the coating layer of the bipolar plate, the SS316L substrate
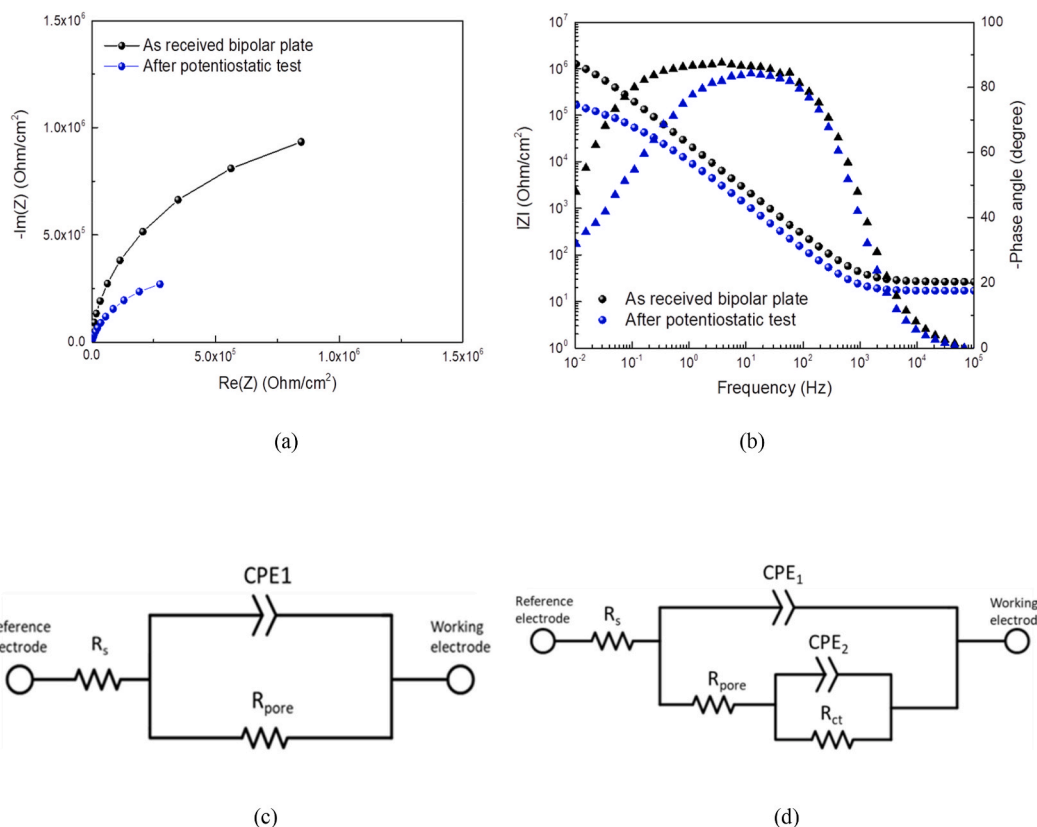
(a)

(b)

(c)

(d)

Fig. 3. Electrochemical impedance spectroscopy test results for bipolar plates before and after potentiostatic polarization tests. (a) Nyquist plots, (b) Bode plots, (c) equivalent circuit diagram of as-received bipolar plate, and (d) equivalent circuit diagram of coated bipolar plate after potentiostatic polarization tests.

Table 2
EIS test results of bipolar plates before and after potentiostatic polarization tests.

	R_s	CPE_1			CPE_2				χ^2
	$(\Omega \cdot cm^2)$		Y_0 $(0 < n < 1)$	$R_{pore} (\Omega \cdot cm^2)$		Y_0 $(0 < n < 1)$	$R_{ct} (\Omega \cdot cm^2)$	$R_{total} (\Omega \cdot cm^2)$	
As-received bipolar plate	26.96	7.278×10^{-6}	0.9621	1.89×10^6	–	–	–	1.89×10^6	8.66×10^{-4}
Bipolar plate after the potentiostatic test	16.97	1.561×10^{-5}	0.9547	3.75×10^4	1.641×10^{-5}	0.4495	4.35×10^5	4.72×10^5	1.19×10^{-4}

corroded in a high-overpotential environment, thereby increasing the reaction area.

3.1.3. Electrochemical impedance spectroscopy

EIS measurements were performed before and after the potentiostatic polarization test. Nyquist and Bode plots of the data obtained from the electrodes of the as-received coated bipolar plate and the coated bipolar plate after the potentiostatic polarization test are depicted in Fig. 3(a) and (b), respectively. Fig. 3(c) shows a one-time equivalent electrical circuit for the as-received coated bipolar plate, where R_s denotes the solution resistance, R_{pore} denotes the pore resistance resulting from the formation of ionic conduction paths across the coating, and CPE_1 denotes the dielectric characteristics of the coating layer [48]. Fig. 3(d) shows a two-time equivalent electrical circuit for the coated bipolar plate after the potentiostatic polarization test. The two-time circuit can explain the occurrence of defects in the coating layer and the exposure of the SS316L substrate after the potentiostatic test. In Fig. 3(d), R_s denotes the solution resistance; CPE_1 denotes the dielectric characteristics of the coating layer; R_{pore} denotes the pore resistance; CPE_2 denotes the constant phase element (CPE) of the double layer; R_{ct} denotes the charge transfer resistance [49,50]. Because a depressed capacitive loop was observed in the Nyquist plot, a CPE was used instead of a capacitor to compensate for the nonhomogeneity of the system frequency. The impedance of a CPE is described by the following Eq. (4):
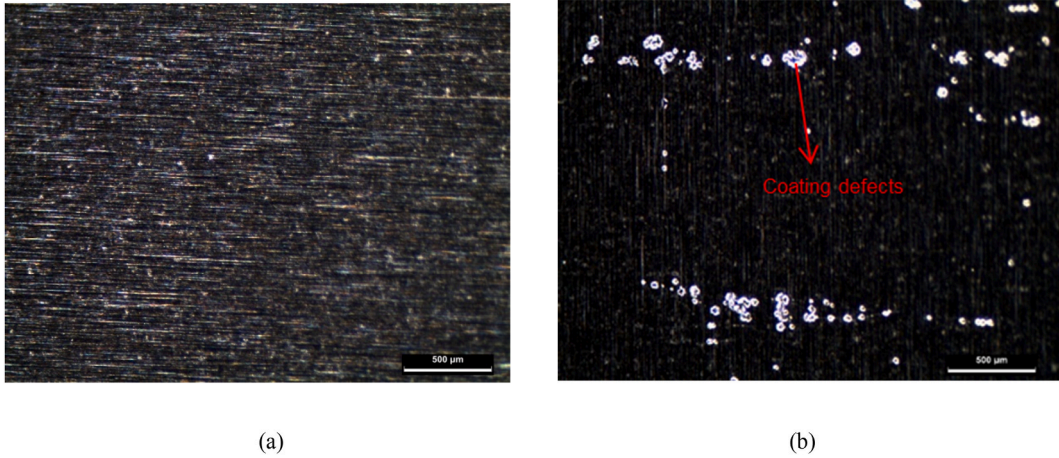
(a)   (b)

Fig. 4. Surface optical microscopy images of bipolar plates: (a) as-received coated bipolar plate (45 ×) and (b) coated bipolar plate after potentiostatic polarization test (45 ×).
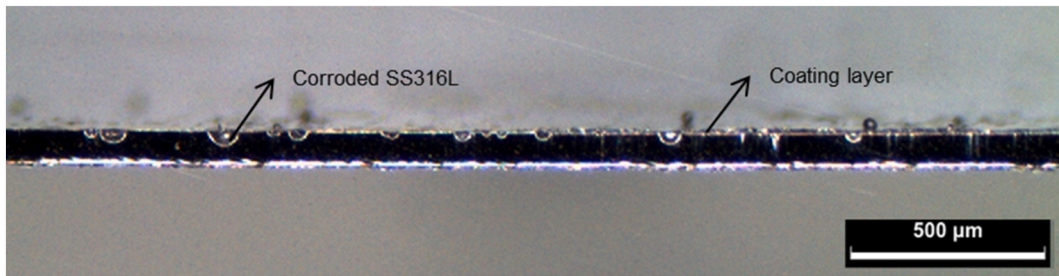

Fig. 5. Cross-sectional optical microscopy image of bipolar plate after potentiostatic polarization test (45 ×).

$$Z_{\mathrm{CPE}} = A^{-1}(j\omega)^{-n}, \tag{4}$$

where A^{-1} denotes the proportionality coefficient (with units $\Omega^{-1}\,\mathrm{s^n\,cm^{-2}}$), ω denotes the angular frequency (rad $\mathrm{s^{-1}}$), $j^2 = -1$ is the imaginary number, and n represents the empirical exponent ($0 \leq n \leq 1$) that measures the deviation from the ideal capacitive behavior [51–53]. The EIS fitting data obtained using the ZSimpWin software are presented in Table 2. The fitting quality of the EIS data was assessed using the chi-squared values (χ^2), which range from 1.19×10^{-4} to 8.66×10^{-4}. These chi-squared values suggest a favorable agreement between the EIS data and the fitting results of the coated bipolar plate specimens. The Nyquist plot provides indication of corrosion resistance through the radius of the capacitive loop, which represents the polarization resistance, as shown in Fig. 3(a). This shows that after the potentiostatic test, the capacitive loop radius for the coated bipolar plate becomes smaller than that for the as-received bipolar plate. Consequently, degradation of the protective coating occurs, thereby decreasing R_{pore}.

Here, R_{pore} can be used to analyze the properties of the coatings. The value of R_{pore} is described by the following Eq. (5) [54]:

$$R_{pore} = \frac{\rho l}{PA}, \tag{5}$$

where ρ denotes the resistivity of the solution within the pores, l and A represent the pore length and area, respectively, and P represents the porosity of the coating. The R_{pore} value of the coated bipolar plate after the potentiostatic polarization test was lower than that of the as-received coated bipolar plate. This result indicates that for the coated bipolar plate, the number of pores and the pore area of the coating increased because of coating degradation after the potentiostatic polarization test. Moreover, as shown in Fig. 3(b), $|Z|$ impedance for the coated bipolar plate after the potentiostatic polarization test is lower than that for the as-received bipolar plate at low frequencies, indicating a lower corrosion resistance [55]. Therefore, the protective effect of the coating on the substrate decreased after the potentiostatic polarization test. In addition, R_{total}, which denotes the total corrosion resistance of the bipolar plate, decreased after the potentiostatic polarization test. In conclusion, in a PEMWE operating environment, where a high overpotential is applied, the corrosion resistance of a coated bipolar plate decreases with an increase in the pore area of the coating.

3.2. Surface analyses

Fig. 4(a and b) shows the surface OM images of the as-received bipolar plate and the coated bipolar plate after the potentiostatic
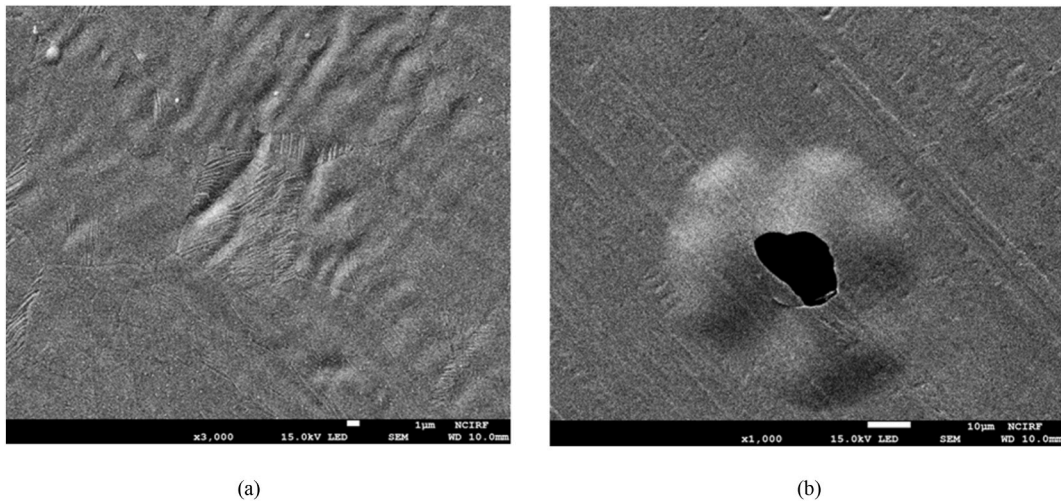
(a)   (b)

Fig. 6. Surface scanning electron microscopy images of bipolar plates: (a) as-received bipolar plate and (b) bipolar plate after potentiostatic polarization test.
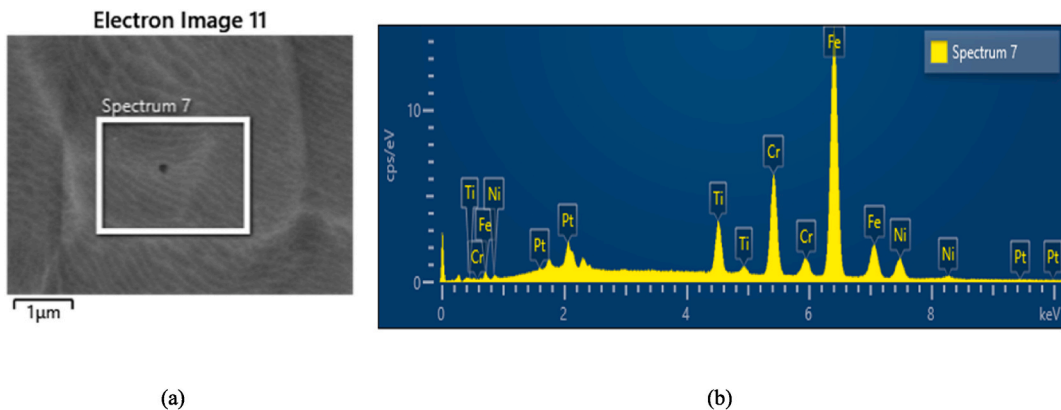

(a)   (b)

Fig. 7. (a) Surface scanning electron microscopy images of the interior of coating defect. (b) Energy-dispersive X-ray spectroscopy results for the interior of the coating defect.

Table 3
EDS results for the material interior of the coating defect shown in Fig. 7.

Element	Composition (Weight %)	Composition (Atomic %)
Ti	5.44	6.41
Cr	15.68	17.01
Fe	65.94	66.59
Ni	9.31	8.95
Pt	3.62	1.05
Total:	100.00	100.00

polarization test at a magnification of 45 times. In the case of the as-received bipolar plate, no visible defects were observed on the surface. However, after the potentiostatic polarization test, coating defects were observed in the coating layer of the coated bipolar plate surface. In comparison, the as-received bipolar plate exhibited a defect-free surface. Furthermore, there was no evidence of corrosion within the coating layer, except for the coating defects. Fig. 5 shows the cross-sectional OM image of the coated bipolar plate after the potentiostatic polarization test at a magnification of 45 times. The results confirmed that the SS316L substrate was corroded in the area where defects occurred in the coating layer, thereby exposing the SS316L substrate to the electrolyte, indicating a penetration risk to the bipolar plate.

Fig. 6 shows the surface SEM images of the as-received coated bipolar and the coated bipolar plate after the potentiostatic polarization test. As shown in Fig. 6(a), multiple droplets and blistering of several micrometers in size were observed on the surface of the
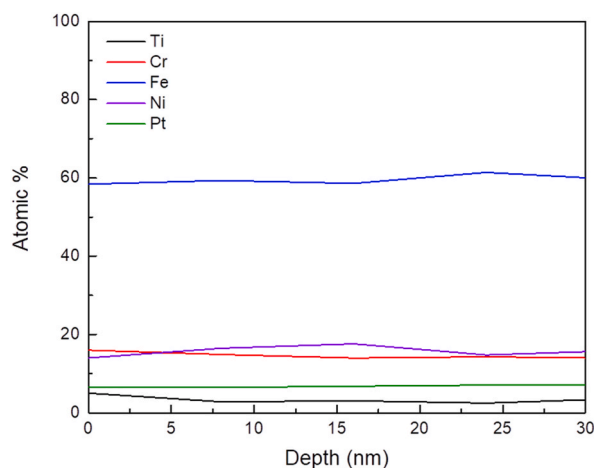
Fig. 8. AES depth profiling analysis (Atomic %) of interior of coating defect.
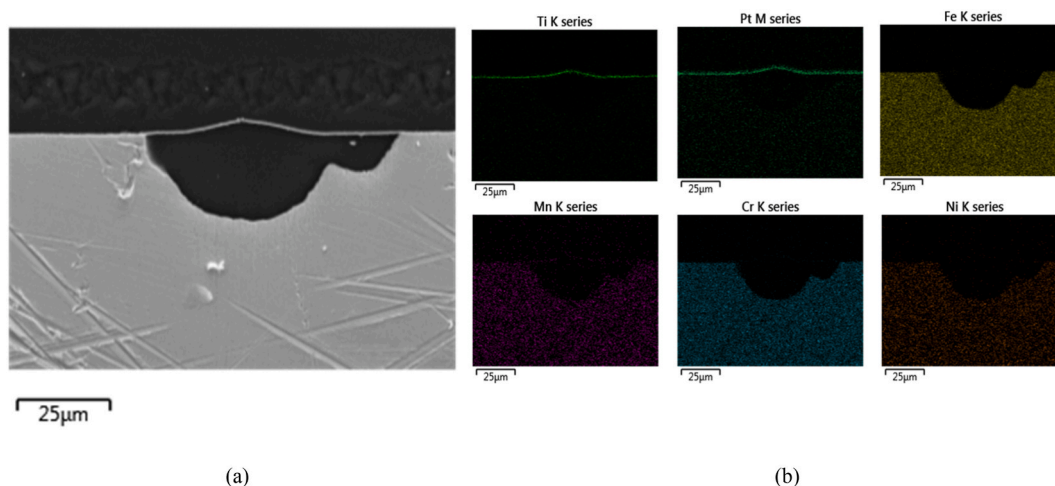

(a)   (b)

Fig. 9. (a) Cross-sectional scanning electron microscopy images of bipolar plate after potentiostatic polarization test. (b) Energy-dispersive X-ray spectroscopy result for bipolar plate after potentiostatic polarization test.

as-received bipolar plate. Blistering, which occurs during the heat treatment process after the PVD process, is considered a vulnerable area with micro voids and micro cracks in the coating [56–58]. In this area, defects could have occurred in the coating layer because the electrolyte may have penetrated the micro cracks, causing corrosion and cracking of the coating and substrate. As shown in Fig. 6 (b), after the potentiostatic polarization test, a coating defect of approximately 10 μm and coating delamination around the defect were observed, and corrosion of the coating layer was not confirmed on the surface of the coated bipolar plate. It is determined that delamination of the coating layer and defects within the coating layer occurred because of pressure generated within the coating layer.

Fig. 7(a) shows the SEM image of the interior of the coating defect that occurred after the potentiostatic polarization test. It was confirmed that corrosion occurred in the material suspected to be SS316L substrate. EDS analysis was conducted to confirm the material interior of the coating defect. The EDS analysis results are presented in Fig. 7(b) and Table 3. The results confirmed that the interior of the coating defect was SS316L because of its high composition ratio of Fe, Ni, and Cr. Fig. 8 shows the AES depth profiling result for the interior of the coating defect. A high composition ratio of Fe, Ni, and Cr compared with that of Ti and Pt was also observed, as shown in Fig. 8, indicating that corrosion of the SS316L substrate occurred after coating degradation. This supports the EDS analysis results. Fig. 9(a and b) shows the cross-sectional SEM image and EDS mapping analysis of the coated bipolar plate after the potentiostatic polarization test. We confirmed that corrosion of the SS316L substrate occurred in the area where defects of the coating layer occurred. Moreover, delamination of the coating layer was also observed in areas where the SS316L substrate had corroded. This delamination can be attributed to the pressure generated within the coating layer and the lack of support for the coating layer due to voids created by the corrosion of the SS316L substrate. Fig. 10 shows the captured image of the *in-situ* OM monitoring video of the bipolar plate surface during the potentiostatic polarization test. The video of Fig. 10 can be downloaded from the website of this Journal. At the beginning of the potentiostatic polarization test, oxygen bubbles were generated on the surface of the coating
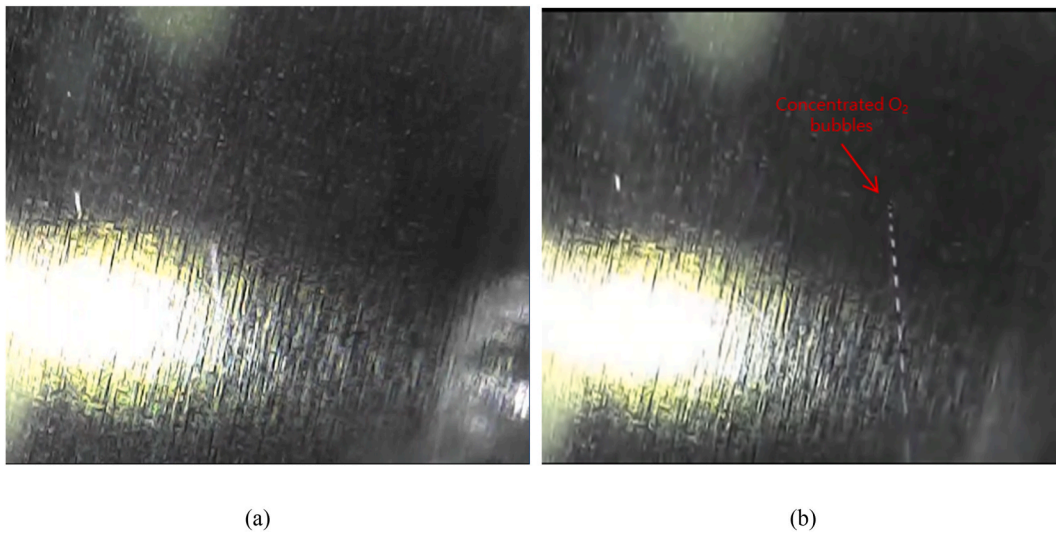
(a)   (b)

Fig. 10. Captured image of *in situ* OM monitoring video of bipolar plate during potentiostatic polarization test: (a) image at the beginning of the test, and (b) image of concentrated oxygen generation.
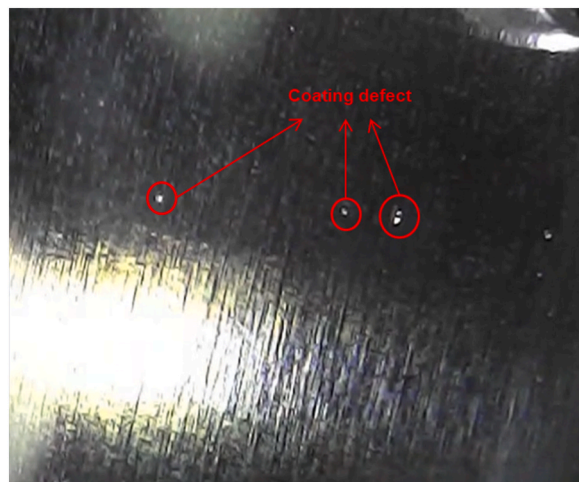

Fig. 11. Surface image of bipolar plate after potentiostatic polarization test.

layer, and coating defects were not visually observed as shown in Fig. 10(a). However, we confirmed that concentrated oxygen bubbles occurred in a specific area, and after the occurrence of concentrated oxygen bubbles, coating defects were also visually observed in that area, as shown in Fig. 10(b). As shown in Fig. 11, we confirmed that defects occurred in the coating layer of the coated bipolar plate in this area after the concentrated generation of oxygen bubbles. Furthermore, we confirmed that the SS316L substrate was exposed to the electrolyte. Therefore, it can be inferred that corrosion of the SS316L substrate occurs after coating defects and delamination of the coating layer. In conclusion, it is determined that electrolyte penetrates into blistering areas, not visible to the naked eye, where micro cracks exist in the coating layer. Subsequently, oxygen gas is generated within the coating layer under high-voltage conditions, leading to delamination and defects in the coating layer due to the pressure of the oxygen gas. Consequently, the substrate is exposed to the electrolyte.

Fig. 12 shows the degradation mechanism of the coated bipolar plate owing to the reaction of oxygen gas generation during the PEMWE operation based on the above-mentioned results. The degradation mechanism of the coated bipolar plates can be divided into two stages: (i) the initial stage, which shows the failure of the coating; (ii) the final stage, which shows the corrosion of the substrate. Oxygen gas is generated within the coating layer because of the high-overpotential environment after the electrolyte penetrates the micro pits and micro cracks in the coating layer. The accumulation of oxygen gas within the coating layer results in the breakdown and delamination of the coating layer because of the pressure of oxygen gas. Finally, the electrolyte contacts the SS316L substrate through the area where the coating layer is damaged, and the SS316L substrate with low corrosion resistance is intensively corroded in the PEMWE operating environment with a high overpotential.
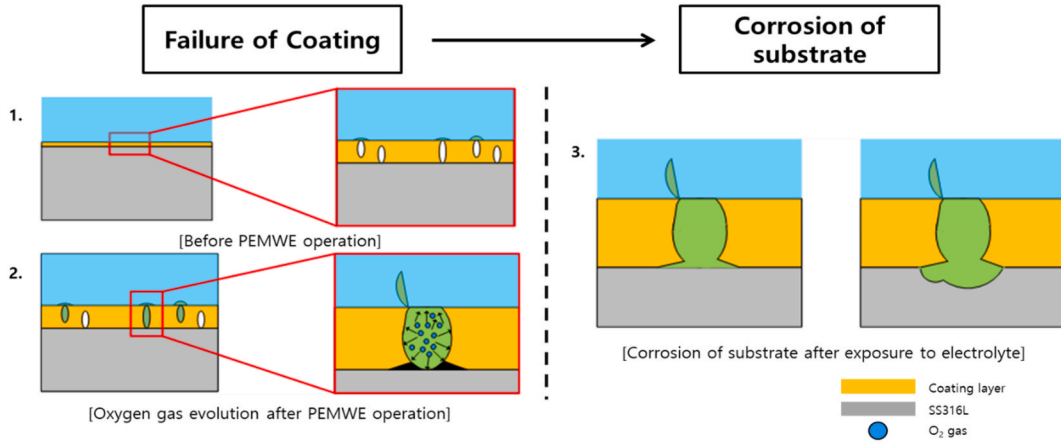
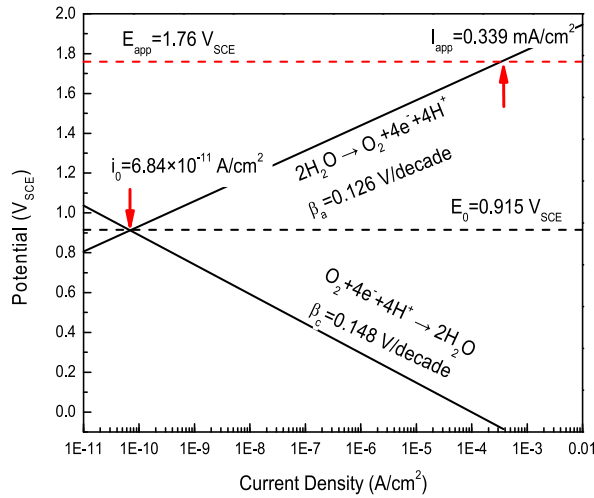**Fig. 12.** Degradation mechanism of coated bipolar plates.

Fig. 13. Tafel plot of oxygen evolution reaction under operating conditions of polymer electrolyte membrane water electrolysis.

3.3. Oxygen generation experiment

To validate the derived degradation mechanism of the coated bipolar plate, we compared the theoretical volume of oxygen gas generated with the experimental volume of oxygen gas obtained through an oxygen generation experiment. When a PEMWE operating potential of 1.76 V_{SCE} is applied, we assume the occurrence of only oxygen generation and corrosion reactions of the SS316L substrate and that the generated oxygen gas follows the ideal gas equation. Because the pH of the PEMWE simulation solution is acidic at 1.25, the OER was determined using the following Eq. (6):

$$2H_2O \rightarrow O_2 + 4e^- + 4H^+, E^0 = 0.989 \text{ V}_{SCE} \ (1.229 \text{ V}_{SHE}). \tag{6}$$
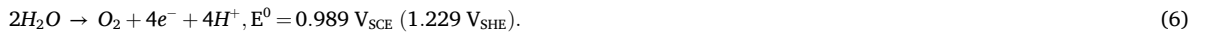
The electrical charge of oxygen generation can be calculated using the volume of oxygen generated under potentiostatic polarization, the ideal gas equation, and Faraday's law of electrolysis calculations and can be described using the following Eq. (7) [59]:

$$Q_{OER} = \frac{zFPV}{RT}, \left(\because Q = nzF, n = \frac{PV}{RT} \right), \tag{7}$$

where z represents the number of electrons participating in the OER, F represents the Faraday constant (96,485C/mol), P represents the pressure, V represents the volume of the generated oxygen gas, R represents the gas constant (0.082 L atm/K·mol), and T represents the temperature of the PEMWE operation environment (338 K).

The theoretical volume of the generated oxygen gas can be derived as follows. First, the Tafel slope of the cathodic reaction is determined by comparing the potentiodynamic polarization curves of the coated bipolar plate in the de-aerated and aerated states of the PEMWE simulation environment. Then, by using the Nernst equation, the standard reduction potential of the oxygen generation

Table 4
Experimental results for oxygen generation.

	Q_{total} (C)	The volume of generated O_2 gas (mL)	Q_{OER} (C)	Q_{corr} (C)	w_{corr} calculation (mg)	w_{corr} experimental (mg)
1	12.61	0.24	3.34	9.27	2.68	2.61
2	12.17	0.25	3.49	8.69	2.51	2.15
3	12.74	0.25	3.49	9.25	2.64	2.35

reaction is calculated under experimental conditions, and the intersection of the extrapolated cathodic polarization curve is determined as the oxygen exchange current density. Finally, assuming that the OER dominates after the inflection point, where the current increases rapidly on the anodic polarization curve of the coated bipolar plate in Fig. 1, the Tafel slope of the anodic reaction is determined, as plotted in Fig. 13. Under the PEMWE operation potential of 1.76 V_{SCE}, the current density of the oxygen generation reaction was calculated as 0.339 mA/cm^2, and 3.66C of electrical charge was contributed to the oxygen generation reaction during 3 h of the potentiostatic polarization test. When the theoretical volume of generated oxygen gas was calculated using Eq. (7), approximately 0.26 mL of oxygen gas was generated theoretically.

The experimental results of the oxygen generation reaction with the application of 1.76 V_{SCE} for 3 h are presented in Table 4. When the electrical charge of oxygen generation is subtracted from the total electrical charge, the electrical charge of SS316L corrosion is calculated. The amount of corrosion of SS316L was determined using the following Eq. (8) [42]:

$$w_{corr} = \frac{E.W. \times Q_{corr}}{zF}, \tag{8}$$

where Q_{corr} denotes the electrical charge of corrosion, *E.W.* denotes the equivalent weight, z represents the number of electrons participating in the corrosion reaction, and F represents the Faraday constant (96, 485C/mol). The experimental results show an average of 0.247 mL of generated oxygen, which is similar to the corresponding theoretical volume of generated oxygen gas. In addition, the corrosion amount of SS316L in the experiment was also similar to the calculated corrosion amount. These similarities in the theoretical and experimental results verify oxygen gas generation and corrosion of the SS316L substrate in the coated bipolar plate during the PEMWE operation.

4. Conclusion

This study investigated the degradation mechanism and corrosion properties of a coated bipolar plate used in a PEMWE stack through electrochemical tests, OM, SEM/EDS, AES, *in situ* OM monitoring, and oxygen generation experiments. On the basis of the experimental results, the following conclusions can be drawn.

- The corrosion resistance of the coated bipolar plate is superior to that of the bare SS316L substrate. The coated bipolar plate has a corrosion current density of only 1.68×10^{-8} A/cm^2, which is an order of magnitude lower than that of the bare SS316L substrate (1.94×10^{-7} A/cm^2). Furthermore, the polarization resistance of the coated bipolar plate is four times higher than that of the bare SS316L substrate. However, in the PEMWE operating environment, coating defects occurred, increasing the porosity of the coating and reducing its protective efficiency, thereby reducing the corrosion resistance of the coated bipolar plate.
- The degradation mechanism of the coated bipolar plate is derived as follows: During magnetron sputtering, blistering forms in the coating layer, and the electrolyte penetrates the blistering. In a high-voltage PEMWE operating environment, oxygen gas is generated inside the coating layer, and delamination and defects occur because of the pressure of this gas. After the occurrence of defects in the coating layer, the SS316L substrate is exposed to the electrolyte, accelerating corrosion in the high-voltage environment.

CRediT authorship contribution statement

Sin-Jae Kang: Writing – original draft, Visualization, Investigation, Formal analysis, Conceptualization. **Geon-Il Kim:** Methodology, Formal analysis. **Seung-Hyun Kim:** Methodology, Formal analysis. **Ji-Han Lee:** Resources. **Jeong-Soo Kim:** Resources. **Seong-Un Im:** Resources. **Yeon-Soo Kim:** Resources. **Jung-Gu Kim:** Writing – review & editing, Project administration.

Declaration of competing interest

The authors declare that they have no known competing financial interests or personal relationships that could have appeared to influence the work reported in this paper.

Acknowledgments

division.

Appendix A. Supplementary data

Supplementary data to this article can be found online at https://doi.org/10.1016/j.heliyon.2024.e34551.

References

[1] V. Khare, S. Nema, P. Baredar, Solar–wind hybrid renewable energy system: a review, Renew. Sustain. Energy Rev. 58 (2016) 23–33.
[2] A. Sternberg, A. Bardow, Power-to-What? – Environmental assessment of energy storage systems, Energy Environ. Sci. 8 (2) (2015) 389–400.
[3] J. Cui, et al., Performance of niobium nitride-modified AISI316L stainless steel as bipolar plates for direct formic acid fuel cells, Int. J. Hydrogen Energy 42 (16) (2017) 11830–11837.
[4] H. Zhang, et al., Electrochemical properties of niobium and niobium compounds modified AISI430 stainless steel as bipolar plates for DFAFC, Surf. Eng. 35 (11) (2019) 1003–1011.
[5] M. Kim, J. Kim, Optimization model for the design and analysis of an integrated renewable hydrogen supply (IRHS) system: application to Korea's hydrogen economy, Int. J. Hydrogen Energy 41 (38) (2016) 16613–16626.
[6] N.P. Brandon, Z. Kurban, Clean energy and the hydrogen economy, Philos Trans A Math Phys Eng Sci (2017) 375.
[7] E.S. Hanley, J.P. Deane, B.Ó. Gallachóir, the role of hydrogen in low carbon energy futures–A review of existing perspectives, Renew. Sustain. Energy Rev. 82 (2018) 3027–3045.
[8] S.Z. Zhiznin, V.M. Timokhov, A.L. Gusev, Economic aspects of nuclear and hydrogen energy in the world and Russia, Int. J. Hydrogen Energy 45 (56) (2020) 31353–31366.
[9] S. Schiebahn, et al., Power to gas: technological overview, systems analysis and economic assessment for a case study in Germany, Int. J. Hydrogen Energy 40 (12) (2015) 4285–4294.
[10] H. Teuku, et al., Review on bipolar plates for low-temperature polymer electrolyte membrane water electrolyzer, Int. J. Energy Res. 45 (15) (2021) 20583–20600.
[11] M.A. Pellow, et al., Hydrogen or batteries for grid storage? A net energy analysis, Energy Environ. Sci. 8 (7) (2015) 1938–1952.
[12] S. Dunn, Hydrogen futures: toward a sustainable energy system, Int. J. Hydrogen Energy 27 (3) (2002) 235–264.
[13] X. Wang, et al., A cocrystallized catalyst-coated membrane with high performance for solid polymer electrolyte water electrolysis, J. Power Sources 240 (2013) 525–529.
[14] A.S. Aricò, et al., Polymer electrolyte membrane water electrolysis: status of technologies and potential applications in combination with renewable power sources, J. Appl. Electrochem. 43 (2) (2013) 107–118.
[15] P. Millet, et al., Electrochemical performances of PEM water electrolysis cells and perspectives, Int. J. Hydrogen Energy 36 (6) (2011) 4134–4142.
[16] K.E. Ayers, et al., Research advances towards low cost, high efficiency PEM electrolysis, ECS Trans. 33 (1) (2010) 3–15.
[17] M. Carmo, et al., A comprehensive review on PEM water electrolysis, Int. J. Hydrogen Energy 38 (12) (2013) 4901–4934.
[18] P. Medina, M. Santarelli, Analysis of water transport in a high pressure PEM electrolyzer, Int. J. Hydrogen Energy 35 (11) (2010) 5173–5186.
[19] I. Vincent, D. Bessarabov, Low cost hydrogen production by anion exchange membrane electrolysis: a review, Renew. Sustain. Energy Rev. 81 (2018) 1690–1704.
[20] H.-Y. Jung, et al., Performance of gold-coated titanium bipolar plates in unitized regenerative fuel cell operation, J. Power Sources 194 (2) (2009) 972–975.
[21] H. Ito, et al., Effect of flow regime of circulating water on a proton exchange membrane electrolyzer, Int. J. Hydrogen Energy 35 (18) (2010) 9550–9560.
[22] J.-T. Wang, et al., Corrosion behavior of three bipolar plate materials in simulated SPE water electrolysis environment, Int. J. Hydrogen Energy 37 (17) (2012) 12069–12073.
[23] J. Wu, et al., A review of PEM fuel cell durability: degradation mechanisms and mitigation strategies, J. Power Sources 184 (1) (2008) 104–119.
[24] N. Rojas, et al., Coated stainless steels evaluation for bipolar plates in PEM water electrolysis conditions, Int. J. Hydrogen Energy 46 (51) (2021) 25929–25943.
[25] H. Zhang, et al., Performance of Ti–Ag-deposited titanium bipolar plates in simulated unitized regenerative fuel cell (URFC) environment, Int. J. Hydrogen Energy 36 (9) (2011) 5695–5701.
[26] R.A. Antunes, et al., Corrosion of metal bipolar plates for PEM fuel cells: a review, Int. J. Hydrogen Energy 35 (8) (2010) 3632–3647.
[27] Q. Feng, et al., A review of proton exchange membrane water electrolysis on degradation mechanisms and mitigation strategies, J. Power Sources 366 (2017) 33–55.
[28] L. Bertuccioli, et al., Study on Development of Water Electrolysis in the EU, Final Report in Fuel Cells and Hydrogen Joint Undertaking (2014).
[29] C. Davies, M. Barnett, Expanding the extrusion limits of wrought magnesium alloys. The Journal of the Minerals,, Metals & Materials Society 56 (5) (2004) 22–24.
[30] J.-L. Cui, et al., Electrochemical properties of tungsten-alloying-modified AISI 430 stainless steel as bipolar plates for PEMFCs used in marine environment. Acta metallurgica sinica (English letters) 29 (10) (2016) 920–927.
[31] J. Cui, et al., Corrosion resistance of a tungsten modified AISI 430 stainless steel bipolar plate for proton exchange membrane fuel cells, RSC Adv. 6 (37) (2016) 31367–31373.
[32] Y. Liu, et al., *Performance of Nb0.8Zr0.2 layer-modified AISI430 stainless Steel as bipolar Plates for direct formic acid fuel cells*. Acta metallurgica sinica (English letters) 34 (1) (2021) 77–84.
[33] K. Liu, et al., Manufacture of Co-containing coating on AISI430 stainless steel via pack cementation approach for SOFC interconnect, Int. J. Hydrogen Energy 44 (57) (2019) 30328–30338.
[34] Y.F. Cui, et al., Electrochemical properties of niobium modified AISI316L stainless steel bipolar plates for direct formic acid fuel cell. Fuel cells – from fundamentals to systems 17 (5) (2017) 698–707.
[35] S. Sun, et al., Investigations on degradation of the long-term proton exchange membrane water electrolysis stack, J. Power Sources 267 (2014) 515–520.
[36] X. Wang, et al., The influence of Ferric ion contamination on the solid polymer electrolyte water electrolysis performance, Electrochim. Acta 158 (2015) 253–257.
[37] A. Kumar, M. Ricketts, S. Hirano, Ex situ evaluation of nanometer range gold coating on stainless steel substrate for automotive polymer electrolyte membrane fuel cell bipolar plate, J. Power Sources 195 (5) (2010) 1401–1407.
[38] Y. Wang, D.O. Northwood, Effect of substrate material on the corrosion of TiN-coated stainless steels in simulated anode and cathode environments of proton exchange membrane fuel cells, J. Power Sources 191 (2) (2009) 483–488.
[39] A.S. Gago, et al., Low cost bipolar plates for large scale PEM electrolyzers, ECS Trans. 64 (3) (2014) 1039–1048.
[40] P. Lettenmeier, et al., Low-cost and durable bipolar plates for proton exchange membrane electrolyzers, Sci. Rep. 7 (1) (2017) 44035.
[41] S. Stiber, et al., *Long-Term Operation of Nb-coated stainless steel bipolar Plates for proton exchange membrane water electrolyzers*. Advanced energy and sustainability research 3 (8) (2022) 2200024.
[42] D.A. Jones, Principles and prevention of corrosion, prentice Hall, Inc. 2 (1996) 168.
[43] A.S. Gago, et al., Protective coatings on stainless steel bipolar plates for proton exchange membrane (PEM) electrolysers, J. Power Sources 307 (2016) 815–825.

[44] S.H. Ahn, et al., A study on the quantitative determination of through-coating porosity in PVD-grown coatings, Appl. Surf. Sci. 233 (1–4) (2004) 105–114.

[45] H.-G. Kim, et al., Electrochemical behavior of diamond-like carbon films for biomedical applications, Thin Solid Films 475 (1–2) (2005) 291–297.

[46] N.D. Nam, et al., Corrosion protection of CrN/TiN multi-coating for bipolar plate of polymer electrolyte membrane fuel cell, Thin Solid Films 519 (20) (2011) 6787–6791.

[47] M. Långberg, et al., Redefining passivity breakdown of super duplex stainless steel by electrochemical operando synchrotron near surface X-ray analyses, npj Mater. Degrad. 3 (1) (2019).

[48] Y.-S. Choi, et al., A comparison of the corrosion resistance of Cu–Ni–stainless steel multilayers used for EMI shielding, Surf. Coating. Technol. 201 (6) (2006) 3775–3782.

[49] J.G. Kim, W.S. Hwang, Tribological behavior of multilayered WC-Ti 1-x Al x N coatings deposited by cathodic arc deposition process on high speed steel. Corrosion science and technology 5 (2) (2006) 52–61.

[50] N.D. Nam, et al., Corrosion protection of Ti/TiN, Cr/TiN, Ti/CrN, and Cr/CrN multi-coatings in simulated proton exchange membrane fuel cell environment, Thin Solid Films 545 (2013) 380–384.

[51] P.Q. Zhang, et al., A pitting mechanism for passive 304 stainless steel in sulphuric acid media containing chloride ions, Corrosion Sci. 34 (8) (1993) 1343–1354.

[52] D.Y. Lee, W.C. Kim, J.G. Kim, Effect of nitrite concentration on the corrosion behaviour of carbon steel pipelines in synthetic tap water, Corrosion Sci. 64 (2012) 105–114.

[53] D.A. López, S.N. Simison, S.R. de Sánchez, The influence of steel microstructure on CO2 corrosion. EIS studies on the inhibition efficiency of benzimidazole, Electrochim. Acta 48 (7) (2003) 845–854.

[54] S.-J. Ko, et al., Effect of surface conditions on the localized corrosion of copper tubes, Mater. Chem. Phys. 302 (2023) 127747.

[55] J.-S. Yoo, S.-J. Ko, J.-G. Kim, Effect of chromium on microstructure and corrosion behavior of high-Cr white cast irons used in coal-fired power plant desulfurization facilities. International journal of metalcasting 18 (2) (2024) 1664–1676.

[56] P. Bras, J. Sterner, C. Platzer-Björkman, Investigation of blister formation in sputtered Cu2ZnSnS4 absorbers for thin film solar cells, J. Vac. Sci. Technol. A: Vacuum, Surfaces, and Films 33 (6) (2015) 61201.

[57] P. Steyer, S. Anderbouhr, P. Jacquot, Effect of Ni interlayer on corrosion behaviour of crn pvd coating deposited onto plastic mould steels, Surf. Eng. 17 (4) (2001) 327–331.

[58] N. Gong, et al., Interfacial hydrogen-related species in low-vacuum-deposited coatings on extrinsic substrates: insights from experimental and theoretical studies, Mater. Today Commun. (2023) 34.

[59] O.G. Martinsen, S. Grimnes, Bioimpedance and Bioelectricity Basics, Academic Press, 2011.